Chemosphere 363 (2024) 142935

Contents lists available at ScienceDirect

Chemosphere

journal homepage: www.elsevier.com/locate/chemosphere

Mixing behaviour and sources of Ag, Pd, and other trace elements in the Estuary and Gulf of St. Lawrence under winter conditions

Duc Huy Dang [a,b,*], Wei Wang [a,1], Dario Omanović [c], Alfonso Mucci [d]

[a] School of the Environment and Department of Chemistry, Trent University, Peterborough, Canada
[b] Water Quality Center, Trent University, Peterborough, Canada
[c] Ruđer Bošković Institute, Division for Marine and Environmental Research, HR-10002, Zagreb, Croatia
[d] Geotop and Department of Earth and Planetary Sciences, McGill University, Montreal, QC, Canada

HIGHLIGHTS

- Contrasting estuarine mixing behaviour of trace and ultratrace elements in winter.
- Complex biogeochemical processes in oxygen-depleted bottom water.
- Dissolved Pt remobilization is related to organic matter remineralization.
- Higher Pt/Pd molar ratios than the oceanic signature indicate atmospheric deposition.

GRAPHICAL ABSTRACT

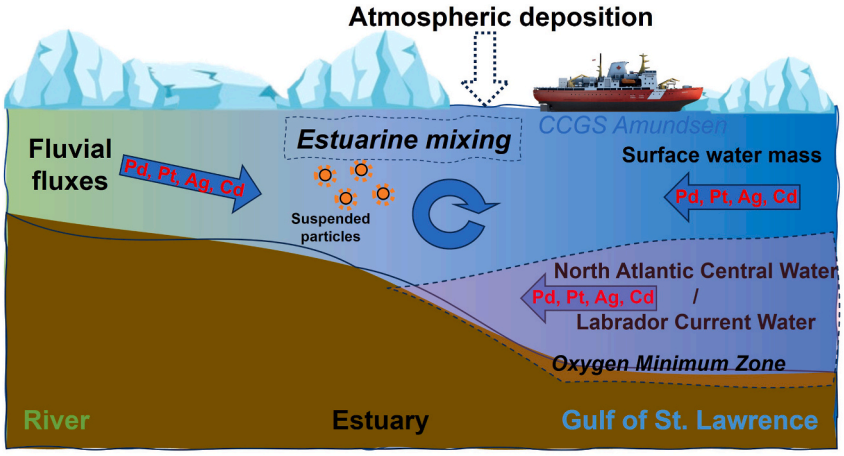

ARTICLE INFO

Handling Editor: Milena Horvat

Keywords:
Silver
Palladium
Estuary
Oxygen minimum zone
Winter

ABSTRACT

The marine chemistry of platinum group elements is poorly documented despite robust evidence of their widespread emissions and deposition around the globe. Here, we report the concentrations and discuss the geochemical behaviours of Ag, Pd and other trace and ultra-trace elements in the Estuary and Gulf of St. Lawrence (EGSL). We highlight the contrasting mixing behaviours of these elements, i.e., conservative (Cd, Re) vs. non-conservative (Ag, Pd), in samples collected during the winter and under ice-covered conditions. We ascribe the contrasting geochemical behaviour of these elements to their differential affinity for reactive surfaces carried into the estuary from the frozen watersheds. We also report an increase of the concentrations of Ag (up to 40 pmol L^{-1}), Pd (up to 10 pmol L^{-1}) and Pt (up to 0.4 pmol L^{-1}) in the bottom and oxygen-depleted waters of the Gulf of St. Lawrence (GSL). A strong correlation between dissolved Pt concentrations and the stable carbon isotopic composition of the dissolved inorganic carbon (δ^{13}C-DIC) suggests that the increased mobility of Pt may

* Corresponding author. School of the Environment and Department of Chemistry, Trent University, Peterborough, Canada.
E-mail address: huydang@trentu.ca (D.H. Dang).
[1] Present address: Department of Earth Sciences, University of Manitoba, Winnipeg, Canada.

https://doi.org/10.1016/j.chemosphere.2024.142935
Received 21 May 2024; Received in revised form 5 July 2024; Accepted 23 July 2024
Available online 23 July 2024

result from the aerobic mineralization of organic carbon or the oxidation of Pt-bearing organic complexes. Molar Pt/Pd ratios in the three water masses that compose the water column in the EGSL highlight a potential influence of anthropogenic sources near urban centers. The signature of continental end-members will be required to confirm the impacts of road traffic on the estuarine geochemistry of these elements.

1. Introduction

The warming climate and modifications in oceanic circulation patterns generate significant environmental changes in the physical and chemical properties of coastal and estuarine ecosystems (Jutras et al., 2023a; Toggweiler and Russell, 2008). The dearth of continuous, all-season environmental data constitutes a significant challenge in documenting ongoing changes in biogeochemical processes globally (Fischer et al., 2021). The winter and ice-covered conditions in high-latitude regions and the lack of suitable sampling infrastructures for these conditions severely hamper access to these data, even though geochemical processes in winter may differ significantly from those in other seasons (Block et al., 2019; Kreyling et al., 2019). Hence, documenting estuarine processes during the winter is particularly important because our understanding of the sources, transport mechanisms and fate of the elements delivered from the continents to the global ocean may be biased by knowledge generated from data acquired during warmer seasons. Consequently, global, marine, elemental budgets might be incorrect because of over- or under-estimated fluvial fluxes (Dang et al., 2022b).

Winter conditions also greatly influence the distribution and timing of the deposition of elements subjected to long-range atmospheric transport. For example, the seasonality of atmospheric Pb deposition in high-latitude regions and the variability of its sources are well documented (Bazzano et al., 2016). Likewise, the long-range transport of Hg and the impact of climate change on its deposition and transfer to the biota have been intensely studied in remote and polar regions (Braune et al., 2015; Chételat et al., 2022; McConnell et al., 2019). In contrast, emerging inorganic contaminants like the platinum group elements (PGEs: Os, Ir, Ru, Rh, Pt and Pd) have received less attention despite solid evidence of their deposition in high-altitude and polar regions (Barbante et al., 2001; Moldovan et al., 2007; Rauch et al., 2005b).

In spite of the global-scale contamination of the terrestrial, aquatic and atmospheric reservoirs from platinum-based catalytic converters (Chen et al., 2009; Rauch et al., 2005a), the PGEs remain among the least studied elements in estuarine and marine waters, leading to a limited understanding of their geochemistry and their impacts on the biota (Abdou et al., 2020; Monteiro et al., 2021). Here, we report dissolved Pd concentrations in the Estuary and Gulf of St. Lawrence (EGSL) from samples collected during a winter oceanographic expedition. We relate the estuarine geochemistry of Pd to that of elements of similar reactivity (e.g., Ag for its propensity to form dissolved chloro-complexes) but also a series of other trace elements whose estuarine mixing behaviours have been more or less well documented (e.g., Cr, Ni, Pb, Re, Zn). The objective is to explore changes in their geochemical behaviours during estuarine mixing of surface waters along the St. Lawrence Estuary (SLE) and within the deep and oxygen-depleted waters of the Gulf of St. Lawrence (GSL). We use the stable oxygen isotopic composition of the water ($\delta^{18}O$–H_2O) and the stable carbon isotopic composition of the dissolved inorganic carbon ($\delta^{13}C$-DIC) together with conventional temperature-salinity diagrams to track the various water masses and elucidate the biogeochemical processes responsible for the distribution of PGEs throughout the EGSL. Note that the geochemical behaviour of other elements in the EGSL has already been addressed in previous publications, e.g., rare earth elements (REEs) and Fe (Dang et al., 2022b), Pt and Cd (Dang et al., 2022a). These results will help frame a better understanding of how the suite of targeted trace and ultra-trace elements behave in the ESGL under winter and ice-covered conditions.

2. Materials and methods

2.1. The Estuary and Gulf of St. Lawrence and their winter water masses

The EGSL connects the Great Lakes (>20% of the world's freshwater reserves) to the North Atlantic Ocean. The St. Lawrence River starts its course at the northeastern tip of Lake Ontario, then converges with the Ottawa River near the Island of Montréal and discharges its freshwater into the SLE downstream of Québec City (Fig. 1). The estuary extends 400 km to Pointe-des-Monts where it widens into the GSL. Traditionally, the SLE is divided into two segments based on its bathymetry and hydrographical features. The Upper St. Lawrence Estuary (USLE) extends from Île d'Orléans to Tadoussac, near the mouth of the Saguenay Fjord (SF). This segment is relatively narrow and mostly shallow, with depths typically less than 30 m. Because of the shallow, rugged bathymetry and strong currents, it displays a strong lateral (horizontal) salinity gradient but the water column is only weakly stratified (El-Sabh and Silverberg, 1990). A maximum turbidity zone is typically found at the head of the USLE where complex density-driven currents combine with resuspended sediments, leading to elevated suspended particle concentrations (up to 98 mg L^{-1} in winter 2020, Dang et al., 2022b; Silverberg and Sundby, 1979). The USLE connects to the much deeper (>300 m) and more strongly stratified Lower St. Lawrence Estuary (LSLE) near Tadoussac. The latter extends to Pointe-des-Monts (Fig. 1A) where it opens up into the GSL.

The Anticosti Gyre is found in the northwestern GSL, adjacent to the mouth of the LSLE, and is formed as the westbound oceanic currents circulate through the Jacques-Cartier Strait (north of Anticosti Island) toward Sept-Iles and converge with the water discharging from the LSLE and flowing in the opposite direction (Fig. 1). The deepwater port of Sept-Iles is the largest mineral port in North America and its city hosts significant historical and ongoing iron- and aluminium-ore processing industries.

The Laurentian Channel, the dominant bathymetric feature of the LSLE and GSL, is a submerged 1280-km long valley that extends from the head of the LSLE to the edge of the eastern North American continental shelf. The northeastern Gulf region, on the northern side of the Laurentian Channel, comprises various oceanographic features, including the Jacques-Cartier Strait, the Anticosti and Esquiman Channels, the Mécatina Trough and the Strait of Belle Isle. The water circulation patterns in this region are complex as Atlantic Ocean water enters the GSL via the Cabot Strait, moves northward through the Esquiman Channel, and encounters Labrador Current Water flowing south from the Strait of Belle Isle through the Mécatina Trough. The Magdalen Shallows, south of the Laurentian Channel, is a vast underwater plateau. Because of the limited depth (<100m) and the strong currents flowing out of the main channel, the current in the Shallows is not as strong as in other parts of the GSL (Galbraith et al., 2021).

The annual wintertime surveys of the EGSL waters conducted since 1996 by Fisheries and Oceans Canada (the Atlantic Zone Monitoring Program) reveal long-term climatologic shifts reflected in changes in air temperatures, sea-ice maximum volumes, circulation patterns and variable water mass distribution and composition (Galbraith et al., 2021).

The volume of the GSL surface mixed layer is estimated at 13 100 km^3, corresponding to 39% of the total volume of the GSL. This layer of oxygenated water is a mixture of freshwater (St. Lawrence River, Saguenay Fjord and other smaller tributaries) and ocean water, mainly from the Labrador Current (Fig. 1A). The average freshwater discharge to the EGSL is approximately 17 800 $m^3\ s^{-1}$, of which 12 700 $m^3\ s^{-1}$ (i.

e., *ca.* 60%) originates from the St. Lawrence River (Galbraith et al., 2021).

The deep (>150 m) oceanic water that enters the GSL through Cabot Strait (~470 m deep) is a mixture of North Atlantic Central Water (NACW) and Labrador Current Water (LCW, <5% according to the latest estimate (Jutras et al., 2023a; Gilbert et al., 2005). In contrast, most of the seawater entering the GSL from the shallower (~100m) Strait of Belle Isle is from the Labrador Current. The LCW is cold (−0.7 to 3.2 °C) and well oxygenated (ca. 300 μmol kg^{-1}), whereas the NACW is warmer (>4.4 °C) and oxygen-depleted (155–250 μmol kg^{-1}); the relative contributions of the LCW entering the GSL through Cabot Strait have been decreasing over time reflecting a change in ocean circulation patterns in the northwestern Atlantic (Jutras et al., 2020, 2023b). The eastern retroflection of the Labrador Current at the tip of the Grand Banks (Newfoundland) is responsible for a significant and rapid deoxygenation and warming of bottom LSLE and GSL waters (Claret et al., 2018; Jutras et al., 2020, 2023a).

A Cold Intermediate Layer (CIL, a remnant water mass that forms in the GSL in the winter), flows landward and persists beneath the surface layer throughout the summer. It mixes with the brackish and cooling surface waters in the fall (Galbraith, 2006). The CIL is typically found between 30 and 150 m depth and characterized by a narrow range of temperatures (−0.6 to 1.5 °C) and high oxygen concentrations (ca. 350 μmol kg^{-1}) (Jutras et al., 2020).

2.2. Sample collection

Water samples were collected from 27 stations (Fig. 1) during a research expedition on the *CCGS Amundsen* icebreaker from February 28th to March 14th, 2020. A detailed description of the sampling protocol and water treatment was provided previously (Dang et al., 2022a, 2022b). Briefly, water samples and ancillary physico-chemical parameters were collected using a rosette sampler equipped with 24 12L-Niskin bottles, Seabird SBE-911 Conductivity-Temperature-Depth (CTD) and SBE-11 oxygen probes mounted on a SBE 32 carousel (painted aluminium frame and titanium latches). Although the probes were calibrated by the manufacturer in the months preceding the cruise, discrete samples were taken from the Niskin bottles for laboratory measurements of practical salinity (S_P; Guildline Autosal 8400 salinometer calibrated with IAPSO standard seawater) and dissolved oxygen (DO; Winkler titration as described in Grasshoff et al. (1999)) and the CTD records re-calibrated post-cruise. The temperature and salinity data were later used to determine water density using the function *sw_dens* of the R package *marelac*.

The water samples were collected in Niskin bottles at discrete depths corresponding to the surface (2–3 m), half of the water column depth (intermediate), and approximately 10 m above the seafloor (deep). Stations P1 to P15 are located along the main channel of the EGSL, with P2–P5 in the USLE, P6–P10 in the LSLE and P12–P15 in the GSL (Fig. 1). Three stations (P23, P25 and P26) were located in the open GSL, with P26 and P23, like the P1–P15 section, along the Laurentian Channel. Station P25 was located in the Magdalen Shallows. Samples were also collected in the Saguenay Fjord (P16-18), the Jacques Cartier Strait, north of Anticosti Island (P21–P22), and Sept-Iles Bay (P28–P30).

Overall, data from the 27 stations along the EGSL and at three water depths were used to assess the mixing behaviour of the targeted elements between distinct water masses, including the St. Lawrence River freshwater (station P1), the brackish waters of the Saguenay Fjord (stations P16-18), the surface and deep seawater entering the GSL from Cabot Strait and the Strait of Belle Isle (stations P23-26).

2.3. Water sample treatment and elemental analysis

Upon securing the rosette on deck, water samples were collected directly from the Niskin bottles into pre-cleaned 1-L FEP bottles for ultra-trace analyses. The bottles were then transported to a clean lab for

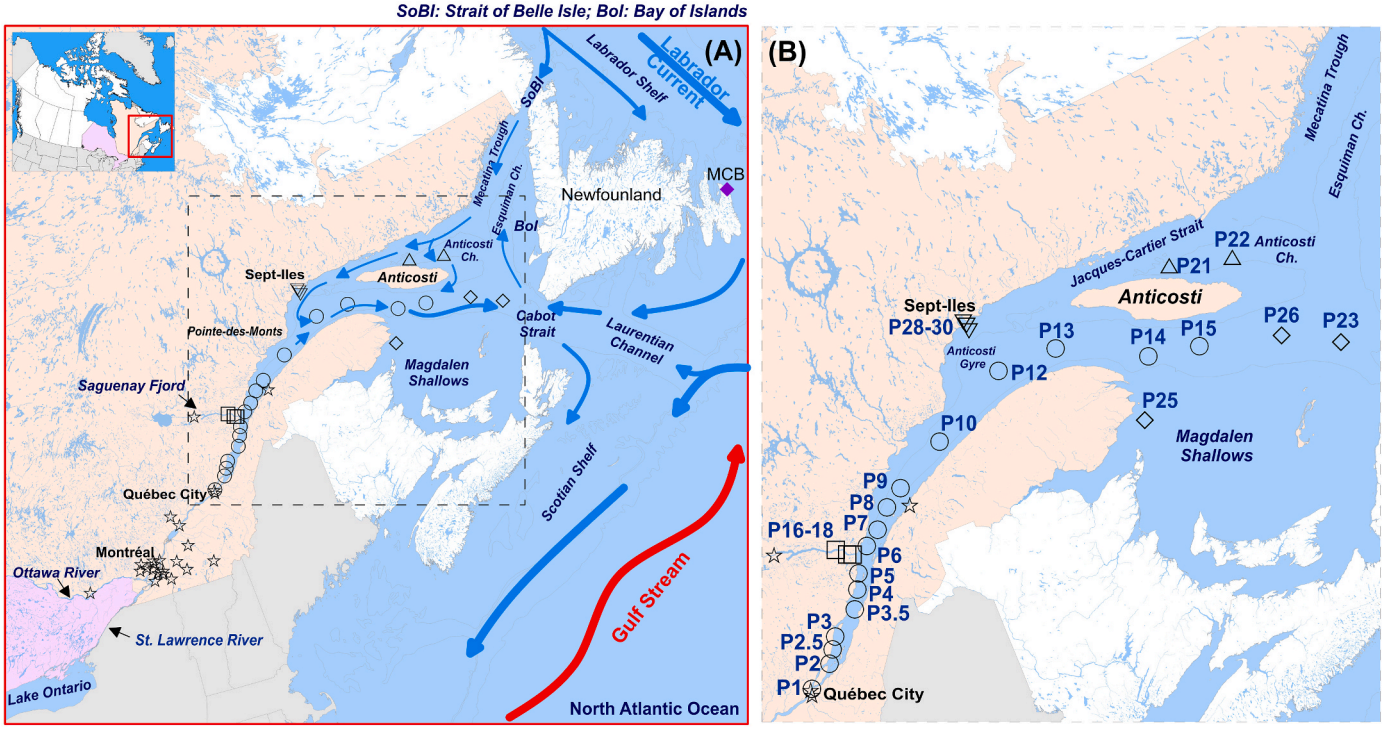

Fig. 1. (A) Map of the Estuary and Gulf of St. Lawrence (EGSL) in eastern Canada, with major surface currents identified for March 2020 (Galbraith et al., 2021) and the location of sampling stations. MCB (Middle Cove Beach) indicates the origin of our in-house standard to calibrate the preconcentration method on the 1-X8 resin. (B) The precise location of sampling stations: Circles identify stations along the main channel of the EGSL, squares are stations in the Saguenay Fjord, diamonds are stations in the GSL, upward triangles are stations in the Jacques Cartier Strait and Anticosti Channel, and downward triangles are stations in the vicinity of Sept-Iles Bay. The star symbols in (A) indicate cities in Québec with populations exceeding 50 000 inhabitants.

further treatment. We followed a strict trace element sampling protocol, as previously detailed by Dang et al. (2022b). Briefly, all bottles were soaked in 10% Trace Metal Grade HNO_3 for a few hours and rinsed several times with ultrapure water (18.2 MΩ cm). These pre-cleaned sampling bottles were further rinsed three times with the sample water before the final fill. In the lab, the water was immediately vacuum filtered through 0.45 μm cellulose nitrate membrane filters mounted on a polycarbonate filter holder (Sartorius). The filtered waters were stored in pre-cleaned 125-mL FEP bottles and acidified to 0.2 % v/v with double-distilled Trace Metal Grade HNO_3.

Trace elements were pre-concentrated on resin columns. The first pre-concentration method, using the Nobias Chelate-PA1 resin, was applied for the analyses of Cr, Ni, Pb, and Zn. This method was described in detail and the concentrations of REEs and Fe were published previously (Dang et al., 2022b). To test the recovery from this pre-concentration protocol for seawater, aliquots of a seawater certified reference material (CRM, CASS-6) were added to different pre-concentration batches (n = 3); the measured concentrations were in consistent agreement with certified values (Table S1).

In the second pre-concentration method, we used the anion exchange resin 1-X8; this method was applied to natural samples and tested with CRMs (fresh and seawater: SLRS-6, CASS-6 and NASS-7) for Ag, Cd, Pd, Re and Zn (Wang et al., 2022). The method calibration confirmed the complete elimination of elements (Sr, Zr, Y) that can cause polyatomic inferences upon the analyses of ^{105}Pd (e.g., $^{89}Y^{16}O$, $^{87}Sr^{18}O$, $^{88}Sr^{16}OH$) and ^{107}Ag (e.g., $^{91}Zr^{16}O$, $^{90}Zr^{16}OH$) by ICP-MS. Sample aliquots of 100 mL were loaded on the columns and the elements were collected in 2 mL of the final eluants, yielding 50-fold preconcentration factors.

The eluted samples from the two resin methods described above were analyzed with a Triple Quadrupole ICP-MS (Agilent 8800 QQQ-ICP-MS) under no-gas mode and collision cell mode (He with kinetic energy discrimination) at the Water Quality Center (Trent University). We only report the data from the no-gas mode given its better sensitivity, i.e., approximately three times based on the counts per second. Nevertheless, the latter data were compared to results from the He-mode analyses to confirm the absence of polyatomic intereferences. Given the high selectivity of the column chemistry, no inteferences were observed. The detailed methodology and QA/QC (using two water CRMs, NIST 1640a and SLRS-6) were described previously (Dang et al., 2022b; Wang et al., 2022). The isotopes selected for ICP-MS analyses are provided in Table 1. Given the 50-fold preconcentration factors, the detection limits of our methodology ranged from 0.14 pmol L^{-1} (Cd) to 4 pmol L^{-1} (Zn).

For the elements with certified concentrations in CASS-6 (Cd, Cr, Ni, Pb and Zn), the measured concentrations were in consistent agreement with the certified values (Table S1). Rhenium concentrations, determined using the isotope dilution method (with ^{185}Re), confirmed a complete column recovery for the CRM seawater (Wang et al., 2022). The measured Re concentrations in the freshwater CRM SLRS-6 was 13.8 ± 0.6 ng L^{-1}, compared to 13.5 ± 0.2 ng L^{-1} reported by an international interlaboratory calibration initiative (Yeghicheyan et al., 2019).

For Ag and Pd, there are no available CRMs. We used an in-house seawater sample collected from Middle Cove Beach (MCB, Newfoundland and Labrador, Fig. 1) to determine the column recovery for these elements based on the standard addition method (Wang et al., 2022). The Ag and Pd concentrations in MCB were previously determined to be 11.1 ± 1.8 pmol L^{-1} and 0.2 ± 0.09 pmol L^{-1} (n = 3), respectively, following a 1000-fold preconcentration procedure on the 1-X8 resin. For this set of samples, we applied a 50-fold preconcentration factor; the detection limits of Ag and Pd were 0.5 and 0.2 pmol L^{-1}, respectively. We conducted five column blanks and determined background contributions of 0.15 pmol and 0.006 pmol, corresponding to blank concentrations of 1.5 pmol L^{-1} and 0.06 pmol L^{-1} for Ag and Pd, respectively.

2.4. Stable isotope analyses

Water samples for the stable oxygen isotopic analysis of the water molecule were taken up directly from the Niskin bottles into 13 mL screw-top plastic test tubes. The stable oxygen isotope ratio, $^{18}O/^{16}O$, was determined using the CO_2 equilibration method on a Micromass AquaPrep system and the CO_2 analyzed on a Micromass IsoPrime universal triple collector isotope ratio mass spectrometer in dual inlet mode at the GEOTOP Light Stable Isotope Geochemistry Laboratory (Université du Québec à Montréal). Data were normalized against two internal reference waters, both calibrated against V-SMOW and V-SLAP. The oxygen isotope measurements are reported on the δ-scale in per mil (‰) relative to Vienna Standard Mean Ocean Water (V-SMOW): $\delta^{18}O(H_2O) = ((^{18}O/^{16}O)_{sample}/(^{18}O/^{16}O)_{VSMOW} - 1) \times 1000$. Based on replicate analyses of the samples, the average relative standard deviation of the measurements was better than 0.05‰.

Water samples for the stable carbon isotopic analysis of the dissolved inorganic carbon (DIC) were taken up directly from the Niskin bottles into 60 mL amber glass bottles without headspace, poisoned with a few crystals of $HgCl_2$ and sealed with a conical plastic screw cap. The $\delta^{13}C$-DIC samples were analyzed at the GEOTOP Stable Isotope Laboratory (Université du Québec à Montréal) using a Micromass Isoprime continuous flow isotope ratio mass spectrometer equipped with a MultiFlow (Isoprime) automated injection system. Carbon isotopic values are reported in per mil (‰) with respect to Vienna PeeDee Belemnite

Table 1
Summary of the analytical protocols applied for the quantification of trace and ultra-trace elements as well as their average concentrations in different end-member water masses of the EGSL.

Elements	Analytical techniques	Resin & measured isotopes		Units	River [b] (n = 3)	GSL surface water [c] (n = 3)	GSL deep water [d]	NACW/LCW [e]
		1-X8	Nobias					
Ag	Preconcentration-ICPMS	^{107}Ag		pmol L^{-1}	9.5 ± 1.7	10.8 ± 3.6	16.0 ± 9.5 (18)	12.9 ± 3.5 (4)
Pd	Preconcentration-ICPMS	^{105}Pd		pmol L^{-1}	0.8 ± 0.8	2.3 ± 1.3	2.7 ± 1.5 (18)	2.6 ± 1.6 (5)
Pt [a]	Voltammetry			pmol L^{-1}	0.46 ± 0.09	0.24 ± 0.03	0.30 ± 0.05 (14)	0.27 ± 0.04 (5)
Pt/Pd					>5	0.10 ± 0.06	0.11 ± 0.07	0.10 ± 0.07
Cd	Preconcentration-ICPMS	^{111}Cd		pmol L^{-1}	73 ± 20	285 ± 42	346 ± 39 (17)	327 ± 38 (5)
Cr	Preconcentration-ICPMS		^{52}Cr	nmol L^{-1}	1.7 ± 0.2	2.0 ± 0.3	1.6 ± 1.0 (17)	1.6 ± 0.1 (3)
Cu	Preconcentration-ICPMS		^{63}Cu	nmol L^{-1}	16.1 ± 2.9	3.2 ± 0.3	2.7 ± 0.06 (17)	2.5 ± 0.05 (4)
Ni	Preconcentration-ICPMS		^{60}Ni	nmol L^{-1}	15.8 ± 3	14.2 ± 6.4	11.2 ± 3.8 (17)	13.6 ± 3.6 (4)
Pb	Preconcentration-ICPMS		^{208}Pb	nmol L^{-1}	0.36 ± 0.11	0.21 ± 0.05	0.2 ± 0.2 (16)	0.3 ± 0.2 (4)
Re	Preconcentration-ICPMS	^{187}Re		pmol L^{-1}	26.9 ± 0.5	35.5 ± 1.4	36.6 ± 0.8 (18)	36.3 ± 1.0 (5)
Zn	Preconcentration-ICPMS	^{66}Zn	^{66}Zn	nmol L^{-1}	48 ± 31	124 ± 83	121 ± 86 (16)	123 ± 56 (5)

[a] Data published by Dang et al. (2022a).
[b] Depth <25m, station P1.
[c] Depth <10m, stations 23, 25, 26.
[d] Depth >150m, stations 6–15, 23–26.
[e] Depth >150m, stations 15, 23 and 26.

(VPDB) referenced to the NBS-19 and LSVEC scale. Two internal reference materials ($\delta^{13}C = -3.41 \pm 0.06$‰ & -19.51 ± 0.05‰ vs VPDB) were used to normalize the results on the NBS19-LSVEC scale. The overall analytical uncertainty (1s) on δ^{13}C-DIC values is better than ±0.1‰.

3. Results and discussion

3.1. Water mass identification in the EGSL under winter conditions

3.1.1. T-S diagram

Discrete water samples are plotted on a T-S diagram, with their respective oxygen concentrations, to identify water masses (Fig. 2); the pattern is consistent with long-term data collected in the GSL for the March period (Galbraith, 2006). Within the surface mixed layer, the transition from the LSLE (density of 1022–1023 kg m^{-3}) to the GSL (density of 1025–1026 kg m^{-3}) is reflected by an increase in salinity and decrease in temperature (blue arrow in Fig. 2); all surface water masses were well oxygenated ([DO] > 310 μmol L^{-1}). The vertical profiles reveal the presence of a CIL-like water mass (temperature ~ 1 °C, S_P ~ 32–33 and density of 1026–1027 kg m^{-3} (Galbraith, 2006; Jutras et al., 2020) and the bottom water of the LSLE and GSL (density >1027 kg m^{-3}) (red arrow in Fig. 2). The CIL is typically mixed with the surface layer in winter, and its presence is more readily identified in the spring by the thermal stratification of the surface layer (Galbraith, 2006).

During the winter 2020 cruise, the CIL was about to form and, thus, was not as distinct as in warmer seasons; it also had lower dissolved oxygen levels ([DO] from 180 to 270 μmol L^{-1}) than previously reported values (i.e., ca. 350 μmol L^{-1}, Jutras et al. (2020)). In contrast, the warmer bottom waters (NACW/LCW) are characterized by very low [DO] (minimum of 54 μmol L^{-1} in March 2020), with the [DO] minimum zone found around the 27.0 kg m^{-3} isopycnal (Fig. 2) (Dang et al., 2022b; Gilbert et al., 2005). Bottom-water [DO] in the Laurentian Channel decrease landward, during our study period, from 117 ± 5 μmol L^{-1} at P15, P23 and P26 to 69 ± 13 μmol L^{-1} at P21, P22, and P7-14 (Dang et al., 2022b; Gilbert et al., 2005). Being isolated from the atmosphere due to the strong water column stratification, the bottom waters of the GSL and LSLE lose oxygen gradually, through respiration and remineralization of organic matter (OM) settling from above, as they flow landward. At depths greater than 150 m, the oxygen lost through microbial respiration in the water column and sediments cannot even be replenished by winter convection but only by weak diffusion from the overlying water or by tidal mixing at the head of the LSLE and Laurentian Channel (Gilbert et al., 2005; Jutras et al., 2020).

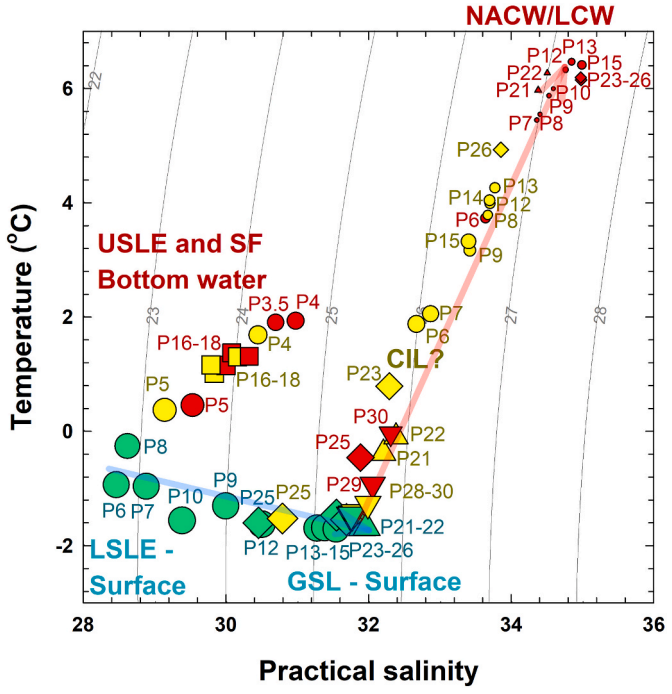

Fig. 2. The T-S diagram identifying water samples collected from the surface (green symbols), intermediate (yellow) and deep (red) layers. The dashed lines represent isopycnals. See the legend in Fig. 1. The symbol sizes are proportional to dissolved oxygen concentrations (54–398 μmol L^{-1}). (For interpretation of the references to colour in this figure legend, the reader is referred to the Web version of this article.)

3.1.2. $\delta^{18}O$–H_2O and δ^{13}C-DIC biplots

Whereas the combined DO and T-S diagram identify parental water masses in the water column, the combined δ^{18}O–H_2O and δ^{13}C-DIC data highlight the water cycle and biological processes governing the respiration of organic carbon and DO depletion in the deep waters of the GSL.

In the St. Lawrence system, the δ^{18}O composition of the river water is relatively uniform (−6 to −7 ‰) from Lake Huron to Montréal, after which the signature drops to −8 ‰ upon the convergence with the Ottawa River (Yang et al., 1996). Likewise, our data at station P1 near Québec City (δ^{18}O of −7.8 ‰, Fig. 3A and S2A) reflects the consistent isotopic signature of the water draining through the main river channel (Barth and Veizer, 1999). The δ^{18}O–H_2O signal is conservative throughout the USLE, as previously reported (Dinauer and Mucci, 2018), and can be represented by $\delta^{18}O\text{–}H_2O = 0.2 \times S_P - 7.82$ ($r^2 = 0.99$, n = 40; Fig. S2A). The Saguenay Fjord (SF) water has a different δ^{18}O–H_2O signature. The S_P of the SF surface water samples collected during this study varied from 9.6 to 19.9 and variations of the δ^{18}O–H_2O along the salinity gradient can be represented by the following relationship ($\delta^{18}O\text{–}H_2O = 0.35 \times S_P - 13.1$, $r^2 = 0.99$, n = 3). Its intercept, −13.1‰, is consistent with the isotopic composition (−12.2 ± 0.2‰) of its main freshwater tributary, the Saguenay River (Delaigue et al., 2020; Yang et al., 1996).

All surface water samples (station P9–P30) of the EGSL ("LSLE – Surface" and "GSL – Surface" in Fig. 3) with S_P ~ 29.4 to 32.0 have nearly constant δ^{18}O–H_2O compositions of −1.8 ± 0.2 ‰ (n = 13, blue area in Fig. 3). In contrast, bottom waters (depth >200m) from station P10 seaward have distinctly higher δ^{18}O–H_2O values of 0.1 ± 0.2 ‰ (n = 9, red area in Fig. 3) at similar salinities ($30.8 < S_P < 35.0$). The latter is a common feature highlighting the mixing of Slope water (itself a mixture of NCAW and LCW) and freshwater, as identified in high-resolution spatial and vertical profiles in the Laurentian Channel on the continental shelf (seaward of Cabot Strait) and the Gulf of Maine, south of the Scotian Shelf (Jutras et al., 2020; Whitney et al., 2020). The δ^{18}O–H_2O data identify four distinct source water masses in the EGSL (Dinauer and Mucci, 2018): the St. Lawrence River freshwater, the Saguenay Fjord tributary, the GSL surface water and the bottom, oxygen-depleted water that originates on the eastern North American continental shelf.

The δ^{13}C-DIC were also significantly different for the various water masses. The DIC in the freshwater of the St. Lawrence River at station P1 (Québec City) has a δ^{13}C value of ca. −2 ‰ (Fig. 3); this signature is ^{13}C-enriched relative to those of its main tributaries (Ottawa River at −9.5 ± 1.7‰ and Lake Ontario at −0.5 to −1‰; Hélie et al., 2002). It is believed that the discrepancy arises due to a slow re-equilibration of the river waters with the atmosphere (Yang et al., 1996). The estuarine mixing behaviour of δ^{13}C-DIC was relatively conservative during our sampling period and follows the following linear relationship: $\delta^{13}\text{C-DIC} = 0.08 \times S_P - 2.13$ ($r^2 = 0.95$, n = 27, Fig. S2B) for all surface water samples (<25 m). This conservative behaviour is uncommon, as most estuarine systems display a non-conservative mixing behaviour (Bouillon et al., 2012). This quasi-conservative mixing behaviour in the EGSL indicates that active sources and sinks of DIC (e.g., respiration, photosynthesis) were negligible during the winter of 2020.

For most marine stations in the GSL (stations P12 seaward), the δ^{13}C-

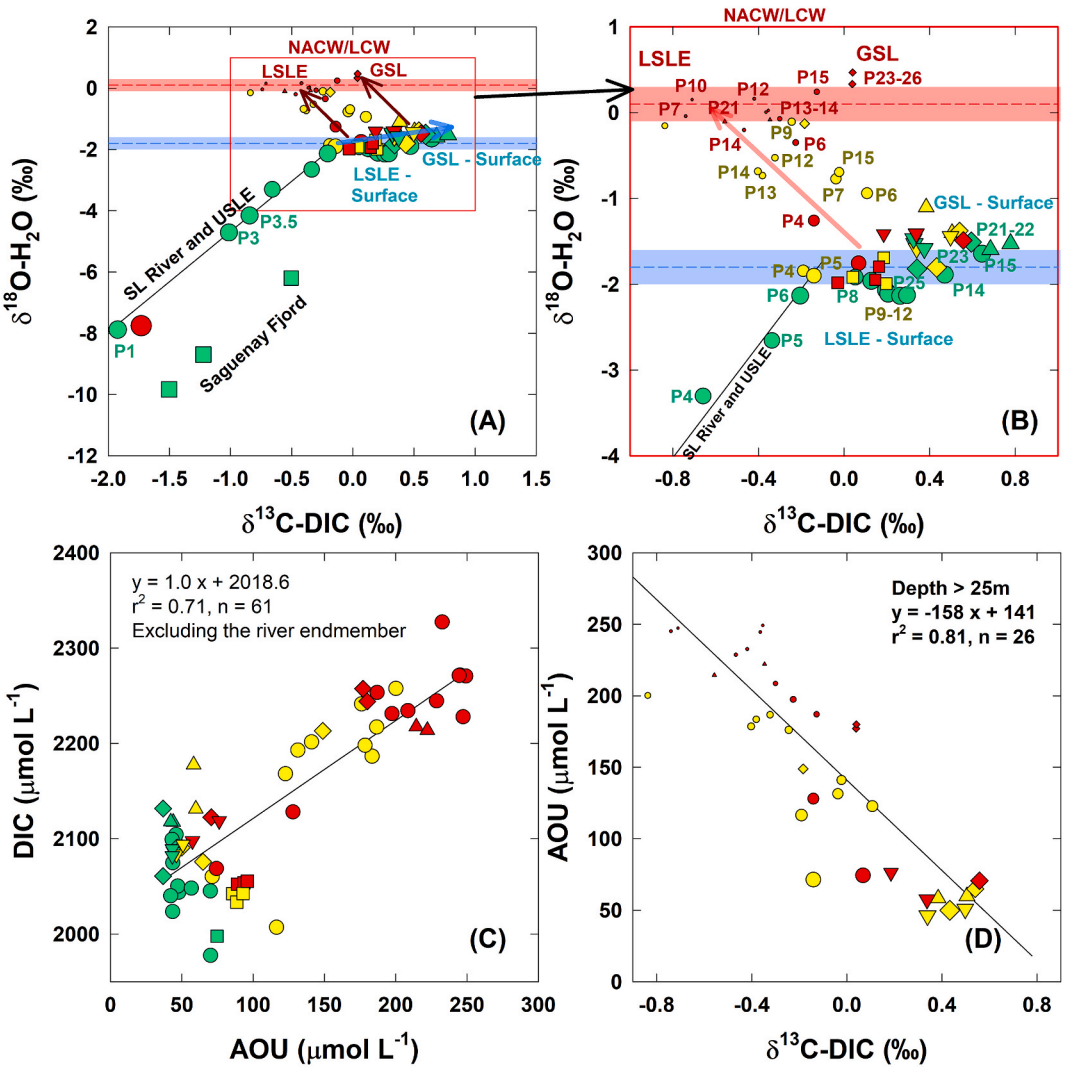

Fig. 3. Biplots of $\delta^{18}O$–H_2O and δ^{13}C-DIC for the entire dataset (A), the LSLE and GSL (B), and the relationship between apparent oxygen utilization (AOU), DIC (C) and δ^{13}C-DIC (D). The symbol sizes are proportional to dissolved oxygen concentrations (54–398 μmol L^{-1}). Refer to previous legends for symbol colours and shapes. (For interpretation of the references to colour in this figure legend, the reader is referred to the Web version of this article.)

DIC composition in surface water was 0.5 ± 0.2 ‰ (n = 11), slightly lower than the values measured along a transect across the Cabot Strait, i.e., 1.1 ± 0.1‰ with a maximum value of 1.5 ‰ (Ji, 2019). In contrast, the subsurface waters (depth >150m) of the EGSL have significantly lower δ^{13}C-DIC values (−0.83 to 0.04 ‰, red arrows in Fig. 3A and B), with higher values in the deep water of the GSL (P15, P23 and P26: 0.1 ± 0.1‰, n = 5) than the LSLE (−0.4 ± 0.2‰, n = 13) (Fig. 3B). We calculated the apparent oxygen utilization (AOU) as the difference between the oxygen solubility (Garcia and Gordon, 1992) at the samples' temperature and salinity and the measured oxygen concentration. In the intermediate and deep waters, i.e., depth >25 m, both DIC and δ^{13}C-DIC values were strongly correlated with AOU (Fig. 3C and D). The production of DIC is directly related to AOU with a slope of 1 (Fig. 3C). The decrease in δ^{13}C-DIC values from 0.5 to 0.6 ‰ at stations P23, P25, P26 and landward with increasing AOU (Fig. 3D) highlights active biogeochemical processes that produce metabolic DIC (oxic microbial respiration of ^{13}C-depleted OM that settles through the water column) as the waters are advected landward (Nesbitt et al., 2023, 2024). We calculated the isotope fractionation (Δ^{13}C-DIC) within the EGSL as the difference between the δ^{13}C-DIC values measured at the most seaward station (P23, 0.54‰) and δ^{13}C-DIC values of each sample; Δ^{13}C-DIC values in the deep water of the GSL reached up to 1.4 ‰ at the head of the LSLE (stations 7 and 8).

In summary, the combination of the T-S diagram with the dual isotope-system approach further confirmed the presence and identity of various water masses in the St. Lawrence system: the St. Lawrence River, the Saguenay Fjord, the surface and bottom waters of the LSLE and the GSL as well as the extent of mineralization processes and metabolic CO_2 production in the bottom waters of the LSLE and GSL.

3.2. *Contrasting estuarine mixing of the elements under winter conditions*

Under the winter conditions of 2020, the estuarine geochemistry of several elements was shown to display a near-conservative mixing behaviour, e.g., Fe and REEs (Dang et al., 2022b), Cd (Fig. 4A) and Pt (Dang et al., 2022a). Rhenium also appears to mix conservatively in the surface waters during the winter (Fig. 4E). The conservative mixing behaviour of these elements has been tentatively explained by the limited supply of reactive particles as well as variable dissolved and particle loads of these elements to the EGSL from the frozen watershed in the winter (Dang et al., 2022a, 2022b). This observation is consistent with the significantly variable particle size distribution of suspended detrital matter in the SLE between the ice-covered and ice-free periods (Fabris et al., 2021). It is, however, important to note the similar mineralogical and elemental composition of the suspended detrital particles in the SLE between seasons and across the estuary.

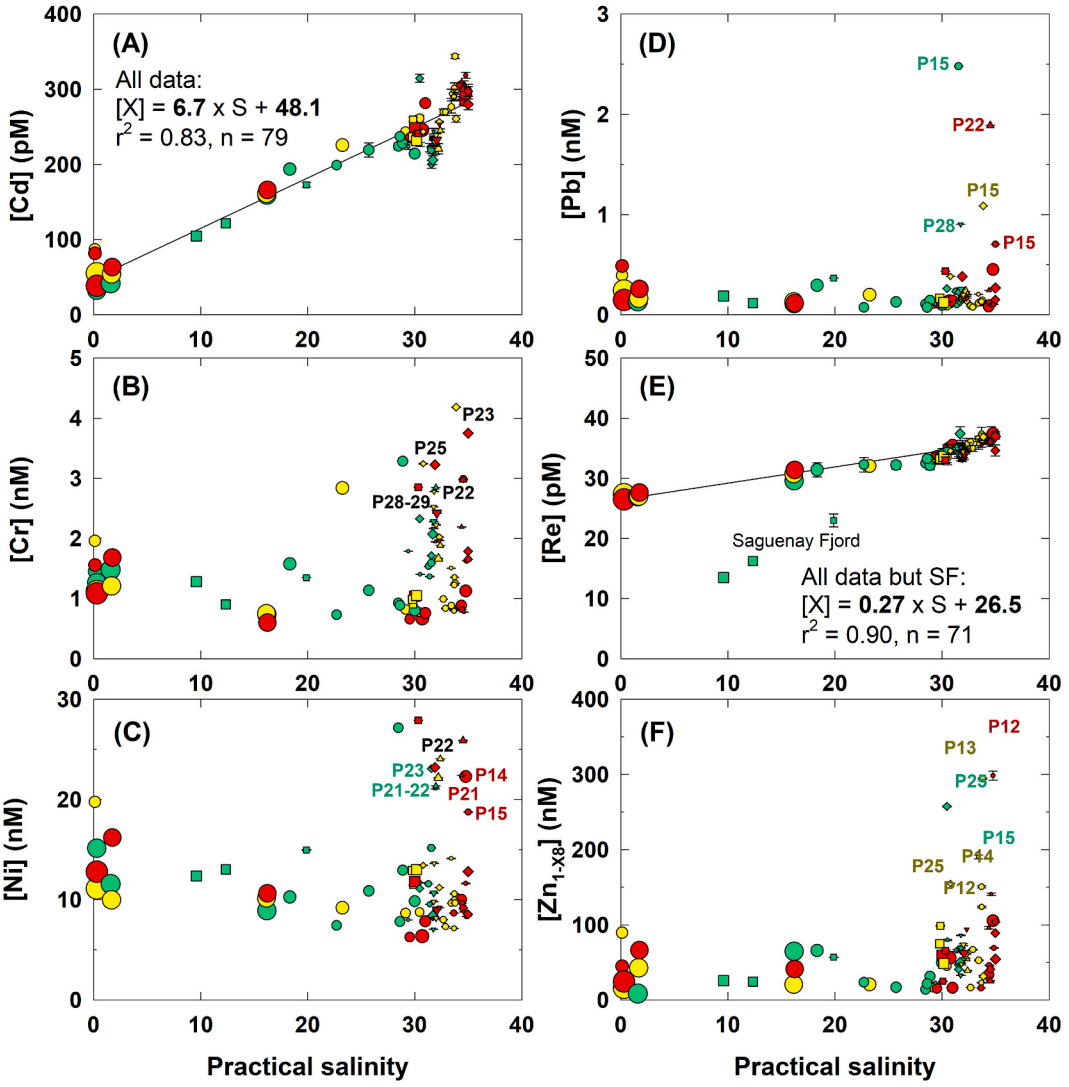

Fig. 4. Concentrations of trace elements (Cd, Cr, Ni, Pb, Re, and Zn) along the EGSL. The full lines are the linear least-squares fit regressions to the data. Refer to previous legends for symbol colours and shapes. (For interpretation of the references to colour in this figure legend, the reader is referred to the Web version of this article.)

Relative to the conservative mixing lines, both Ag and Pd show a positive deviation at intermediate salinities ($S_P \sim 20$) (blue arrows in Fig. 5). The mid-salinity mobilization is coherent with the previously reported behaviour of Ag and Cd in the Gironde Estuary; the maximum dissolved concentrations were observed at S_p between 15 and 20 (Dabrin et al., 2009; Lanceleur et al., 2013). This behaviour has been interpreted as a balance between desorption from particles and dilution by seawater. Four of the targeted elements (Ag, Cd, Pt and Pd) are known to form relatively stable complexes with chloride ions and dissolved OM; the complexation is assumed to be mainly responsible for the remobilization of these particle-bound elements to the dissolved phase in the landward section of the estuary (Cobelo-García et al., 2014; Lanceleur et al., 2013; Waeles et al., 2014). Dilution by seawater beyond this mid-salinity peak explains the decreasing seaward gradient. Nevertheless, Cd (Fig. 4A) and Pt (Dang et al., 2022a) behave conservatively in the EGSL and display no obvious mid-salinity remobilization. These two elements behave similarly in estuarine environments because of their limited reactivity and slow coordination with organic ligands. In contrast, Pd is believed to be chiefly complexed to small hydrophobic ligands (Cobelo-Garcia et al., 2008). This results in a significantly different chemical speciation among these two PGEs under estuarine conditions: whereas Pd is believed to be mainly associated with organic ligands, hydroxychloride complexes of Pt(IV) are dominant (Turner, 2007). In addition, adsorbed Pd is more mobile than Pt, as Pd is sorbed and desorbed rapidly from particles and seems to be the least particle-reactive of the PGEs (Turner et al., 2006). Hence, differences in coordination chemistry and chemical speciation would explain the conservative mixing behaviour of Pt and Cd, whereas Ag and Pd are more readily mobilized to the solution.

3.3. Additional sources of trace elements in the GSL surface waters

In addition to the mid-salinity increase in the concentrations of a few trace elements (e.g., Ag, Pd) in the SLE, we also observed elevated Ag, Pd and Cr concentrations at a few GSL stations relative to the average values in the area (Figs. 4 and 5) and distinct increases in the concentrations of Cr and Pb at stations P28 and P29 (Fig. 4, B and D) near Sept-Iles Bay. Stations P13–P15 and P21-26 in the northeastern GSL also display elevated Ag, Cr and Pd concentrations, whereas Ni concentrations are elevated at stations P21-23 (Figs. 4 and 5).

The open ocean chemistry of Ag is better documented than that of Pd; vertical profiles of Ag in the oceanic water column are similar to Si (i.e., nutrient type), with low concentrations at the surface (1.5–3 pmol kg^{-1}) and significant enrichment at depth (ca. 50 pmol kg^{-1}) (Fischer

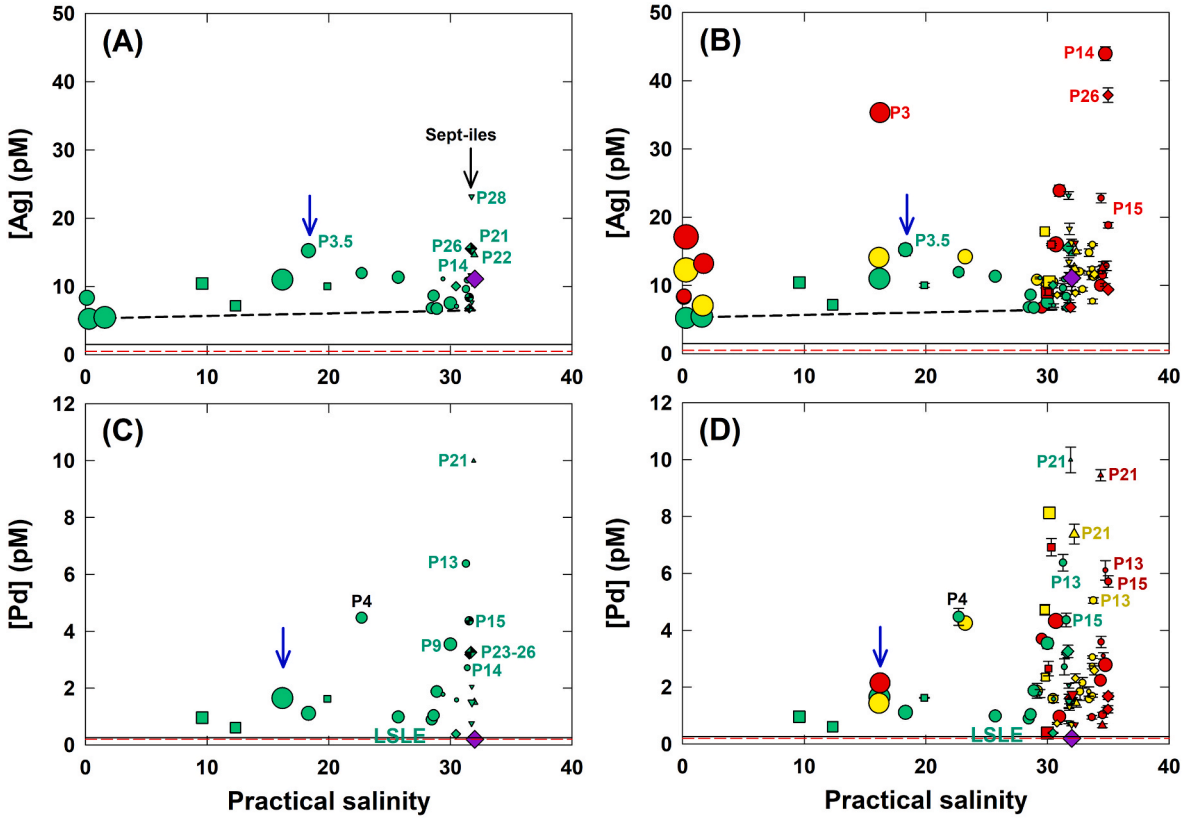

Fig. 5. Concentrations of dissolved Ag and Pd along the EGSL. The left panels show only surface samples (green), whereas the right panels include the intermediate (yellow) and bottom-water (red) samples. The purple diamonds highlight the concentrations of Ag and Pd measured in the in-house standard from Middle Cove Beach collected from the eastern coast of NewFoundland and Labrador. The dashed lines in A and B are the theoretical mixing lines. The symbol sizes are proportional to the suspended particulate matter concentrations (2.1–98 mg L^{-1}). The horizontal dashed red lines show the detection limits of Ag and Pd of the analytical method, based on the ICP-MS sensitivity and preconcentration factors of the resins, see text for more details. The horizontal black lines mark the average of five column blanks. (For interpretation of the references to colour in this figure legend, the reader is referred to the Web version of this article.)

et al., 2018). Dissolved Ag concentrations in the nearshore seawater CRMs CASS-6 and NASS-7 (National Research Council of Canada), taken from the Scotian Shelf off Halifax, have a similar range of concentrations (6.7–10.2 pmol L^{-1}) (Wang et al., 2022) to the open GSL surface water (10.8 ± 3.6 pmol L^{-1}). It is important to note that high-latitude surface water of the North Atlantic is more Ag-enriched than the low-latitude North Atlantic, tropical and South Atlantic water because of a combination of external inputs and water mass circulation patterns (River-a-Duarte et al., 1999). Therefore, it is reasonable to suggest that the dissolved Ag concentrations in the open GSL are consistent with its global distribution pattern, irrespective of potential Ag emission sources around Sept-Iles Bay (station P28).

It is difficult to determine whether the distinct increase in Ag and Pd concentrations observed in surface water at a few GSL stations can be associated with a local geochemical background or anthropogenic emissions. The highest dissolved Pd concentrations were ~10 pmol L^{-1} at station P21 and Ag reached up to 23 pmol L^{-1} at station P28. These concentrations are significantly higher than the average GSL surface water values (2.3 ± 1.3 pmol Pd L^{-1} and 10.8 ± 3.6 pmol Ag L^{-1}, Table 1). For Pd, these concentrations exceed levels observed in the open Pacific and Atlantic Oceans, i.e., 0.04–0.6 pmol L^{-1} (Lee, 1983; Mashio et al., 2022a), but are similar to those of more enclosed coastal systems, e.g., 0.97–1.41 pmol L^{-1} in the Yellow Sea (Liu et al., 2018).

High Ni, Cr and V concentrations in the sediments of the northeastern GSL, especially in the area around the Bay of Islands (BoI) off the west coast of Newfoundland (Fig. 1), were reported by Loring (1979). These anomalies are associated with the glacial erosion of coastal ultrabasic rocks that contain chromite and nickeliferous minerals. Given the lack of sampling resolution in this region, we can only speculate on the origin of the high dissolved Cr and Ni concentrations at stations P21-23. There are permanent surface currents throughout the year coming into the GSL through the Cabot Strait, moving northward through the Bay of Islands and veering west toward Anticosti Island (stations P21, 22, Fig. 1) (Galbraith et al., 2021). Given this circulation pattern, mobilization from the enriched sediments and/or continental runoff reaching the northeastern GSL could be a potential source of these elements.

The higher dissolved Pb and Cr concentrations within Sept-Iles Bay may originate from anthropogenic emissions by local industrial activities and maritime traffic, both of which are well developed in this area. Contamination of the sediments within the bay by As, Cu, Cd, Cr, Hg and Zn has been reported (INREST, 2013); Cr concentrations in sediments across Sept-Iles Bay reach up to 94 mg kg^{-1}, with 52% of the assessed stations exceeding the threshold effect level for marine sediments (52 mg kg^{-1}). Therefore, the contaminated sediments may be a potential source of these trace elements to the water column.

3.4. Trace element concentrations in the deep waters of the EGSL

Among the elements we investigated, only Cd, Cu, and Re have identical concentrations in the deep and surface waters of the GSL at equivalent salinities and fall along the conservative mixing line (Fig. 4), although minor variations can be observed for Cd (Dang et al., 2022a). For other elements (Ag, Pd, Cr, Ni, Pb and Zn), we observed an increase of their concentrations in the oxygen-depleted deep waters relative to the surface waters at equivalent salinities. We have previously ascribed these geochemical behaviours to the microbial mineralization of OM coatings, dissolved oxygen depletion, and the exposure of suspended,

mineral-carrier surfaces. In addition, there might be, under the prevailing reduced oxygen conditions, changes in the redox speciation of Pt as well as processes that could result in the remobilization of trace elements previously bound to organic complexes (e.g., Pt) (Dang et al., 2022a). The diffusion of elements out of the sediments could also contribute as a passive source to the deep water given the very thin sediment oxygen penetration depth (4.1 ± 0.8 mm (Cool, 2022) in the GSL (Gendron et al., 1986; Gobeil et al., 1987; Gobeil and Silverberg, 1989; Lefort et al., 2012).

For Ag and Pd, we observed elevated concentrations in the bottom waters relative to the surface water at the same salinity (Fig. 5); the highest concentrations were observed in the bottom waters at stations P13-15, P21 and P26. The bottom waters at these stations are characterized by low [DO] and a strong shift in δ^{13}C-DIC associated with extensive microbial OM mineralization (Fig. 3). It is, however, unclear whether these high trace element concentrations are a signature of the original water masses (i.e., NACW/LCW) entering the GSL or whether their geochemical cycles have been altered within the GSL because of oxygen depletion. Note that dissolved Pt concentrations in the bottom water of the seaward part of the Laurentian Channel (stations P14, P15, P23 and P26) are similar to those of the Labrador Sea Water (0.27 ± 0.03 pmol L^{-1}) and only slightly higher than the averaged values of the North, Central and South West Atlantic Ocean, i.e., 0.22 ± 0.03 pmol L^{-1} (Dang et al., 2022a; López-Sánchez et al., 2019). This would suggest that the oceanic signature of Pt is preserved despite changes in the biogeochemical properties ([DO], pH) of the water as it enters the GSL and transits landward along the Laurentian Channel.

The nutrient-type behaviour of Ag is well documented in the scientific literature (Fischer et al., 2018). Likewise, we consistently observed higher Ag concentrations in the deep water of the Laurentian Channel (up to 44 pmol L^{-1}, Fig. 5B). In contrast, there is no consensus on the interpretation of vertical oceanic profiles of Pd and Pt. To the best of our knowledge, only two studies have reported vertical profiles of Pd in open ocean water and their interpretations are contrasting: nutrient type (Lee, 1983) vs. scavenging type (Mashio et al., 2022b). The situation is similar for Pt with discrepant behaviours reported: conservative, recycled-type, surface enrichment because of atmospheric inputs, Pt depletion with increasing AOU (Colodner, 1991; Colodner et al., 1993; López-Sánchez et al., 2019). It is intriguing to note that the increased concentration of many of the trace elements (e.g., Pb, Cr, Ni, Zn, Pd, Ag) we measured in the GSL deep water was associated with oxygen-depleted waters. In the intermediate depth and deep waters of the Laurentian Channel, the apparent oxygen utilization (AOU) is strongly correlated ($r^2 = 0.81$, n = 26) to the accumulation of metabolic, ^{13}C-depleted DIC (Fig. 3). Interestingly and likewise, dissolved Pt concentrations (as previously reported by Dang et al. (2022a)), in the intermediate and bottom waters of the GSL are positively and strongly correlated with Δ^{13}C-DIC ($r^2 = 0.67$, n = 24, Fig. 6C). At low Δ^{13}C-DIC (i.e., from 0 to 0.4‰) and low AOU, dissolved Pt concentrations are within the range observed in the Atlantic Ocean (0.22 ± 0.04 pmol L^{-1}, López-Sánchez et al., 2019), implying the preservation of the original oceanic water mass signature. As Δ^{13}C-DIC increases (up to 1.4 ‰), Pt concentrations increase (up to 0.38 pmol L^{-1}). The remobilization of Pt has been associated with the mineralization of Pt-bearing OM, a decrease in Pt-reactive surface sites on suspended particles, and a possible change in its redox speciation, from Pt^{IV} and Pt^{II} species (Dang et al., 2022a).

We did not observe similar correlations between Δ^{13}C-DIC, dissolved Ag and Pd concentrations (Fig. 6A and B). In other words, with the exception of the anomalies observed at P14 and P26, oxic remineralization of OM and other processes (particle interactions and diagenesis) did not seem to affect the Ag geochemistry, as its concentration remained relatively invariant at 13.3 ± 4.9 pmol L^{-1} (n = 46) in the intermediate and deep-water samples throughout the Laurentian Channel (Fig. 6A). Although there might appear to be a positive covariation between the intermediate and bottom water Pd concentrations and Δ^{13}C-DIC, the correlation is not significant (p = 0.17; Fig. 6B). Given the high affinity of Pd for organic complexes in estuarine water (Turner, 2007), one would expect its concentration and mobility to increase as Pd-organic complexes bound to particles are broken down, but other geochemical processes may counter this potential remobilization. Palladium is known for its rapid sorption/desorption kinetics (Turner et al., 2006, see Section 3.2.). Hence, the exposure of mineral surfaces following the microbial degradation of OM coatings on settling mineral particles or newly formed minerals (e.g., Mn oxides from the oxidation of Mn^{+II} and Mn^{+III} diffusing out of the sediments (Oldham et al., 2019; Sundby et al., 1981)) may favor Pd scavenging, an antagonistic effect to its remobilization. This is consistent with our observation that most of the bottom-water samples (lower [DO], red symbols in Fig. 6B) have lower [Pd] concentrations (i.e., more mineralization, less dissolved Pd) than those of the corresponding intermediate water (yellow symbols, higher [DO] and [Pd]). Nevertheless, further studies on the nature and reactivity (e.g., adsorption affinity and capacity) of the settling and authigenic mineral particles in the deep water would be required to validate this hypothesis.

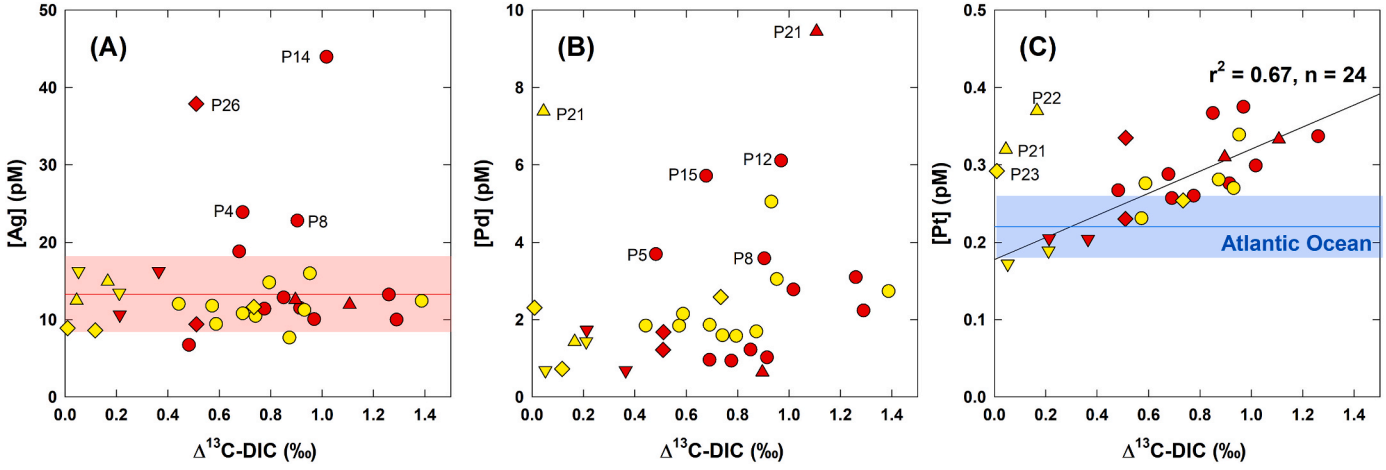

Fig. 6. Concentrations of dissolved Ag, Pd and Pt (data from Dang et al., 2022a) as the function of Δ^{13}C-DIC in the intermediate (yellow) and deep (red) water samples of the Laurentian Channel. The line and red area in A show the average ± sd of Ag concentrations (13.3 ± 4.9 pmol L^{-1} (n = 46)), excluding stations P14 and P26) of the sample set. The line and blue area in C show the average range of concentrations of Pt in the Atlantic Ocean, 0.22 ± 0.04 pmol L^{-1} (López-Sánchez et al., 2019). The regression in C excludes the intermediate waters of stations P21–P23. (For interpretation of the references to colour in this figure legend, the reader is referred to the Web version of this article.)

3.5. Coupling the geochemistry of Pd and Pt in the EGSL

Whereas the estuarine geochemistry of Pd in the EGSL may be significantly different from that of Pt because of their differential chemical reactivities (thermodynamic and kinetic), the deep-water (150m) Pt and Pd concentrations are invariant along the Laurentian Channel (from P6 to P23-26). The Pt concentrations are identical to those reported for the average Atlantic Ocean and LCW (López-Sánchez et al., 2019), but given the lack of data for oceanic Pd concentrations, we can only assume that the extrapolation is also valid for Pd. The average Pd concentration in samples collected below 150 m at stations 15, 23 and 26 in the GSL is 2.6 ± 1.6 pmol L^{-1} (Table 1). Accordingly, the molar Pt/Pd ratio of this presumably oceanic end-member would be 0.10 ± 0.07.

There is increasing evidence of atmospheric deposition of platinum group elements across the globe (Barbante et al., 2001; López-Sánchez et al., 2019). A compilation of data reported by Rauch et al. (2006, 2005b) indicate that the average molar Pt/Pd ratio of atmospheric particles deposited on the North American continent is 0.6 ± 0.3 (n = 31), with a median value of 0.5. Most bottom-water concentration ratios along the Laurentian Channel (especially at stations P10-15, P21, P23-26) are compatible (0.10 ± 0.07) with the oceanic end-member signature (Fig. 7), but samples at stations P22 (Sept-Iles Bay) and P30 (Anticosti Channel) deviate significantly from this ratio, indicating differential geochemical behaviours or sources between the two elements. In the surface waters, whereas the molar Pt/Pd ratios (0.10 ± 0.06) of the open GSL (stations 23, 25 and 26) are similar to the deep ocean signature (0.10 ± 0.07), stations within the St. Lawrence Estuary (USLE and LSLE: P3–P8) and waters collected at stations P28 and P30 (close to the city of Sept-Iles) have ratios >0.2 (red arrows in Fig. 7). The elevated Pt/Pd ratios do not likely result from their differential geochemistry within the estuary, as we observed an increased mobility of Pd in mid-salinity surface water whereas Pt behaved conservatively (see section 3.2.) during mixing, which should translate into a decrease of the Pt/Pd ratio. On the other hand, it is interesting to note that these stations (P3–P8, P28, and P30) are very close to major cities in the Province of Québec (star symbols in Fig. 1); deposition of atmospheric particles originating from urban traffic might drive the surface-water Pt/Pd ratio toward the value of 0.5 (red arrows in Fig. 7). It should be noted, however, that the end-member signature of continental waters, e.g., Great Lakes, is unknown. The molar Pt/Pd in soil samples and road dust collected from a high traffic corridor of Toronto, close to Lake Ontario, range from 0.8 to 2.5 (Wiseman et al., 2016). Hence, whereas we cannot exclude the possibility that the higher Pt/Pd ratios originate from continental runoff (Pt/Pd ≥ 0.5) that is mixed with the marine end-member (Pt/Pd of 0.1), the elevated Pt/Pd ratios most likely originate from the deposition of atmospheric particles emitted from the traffic of larger urban centers of the Great Lakes watershed.

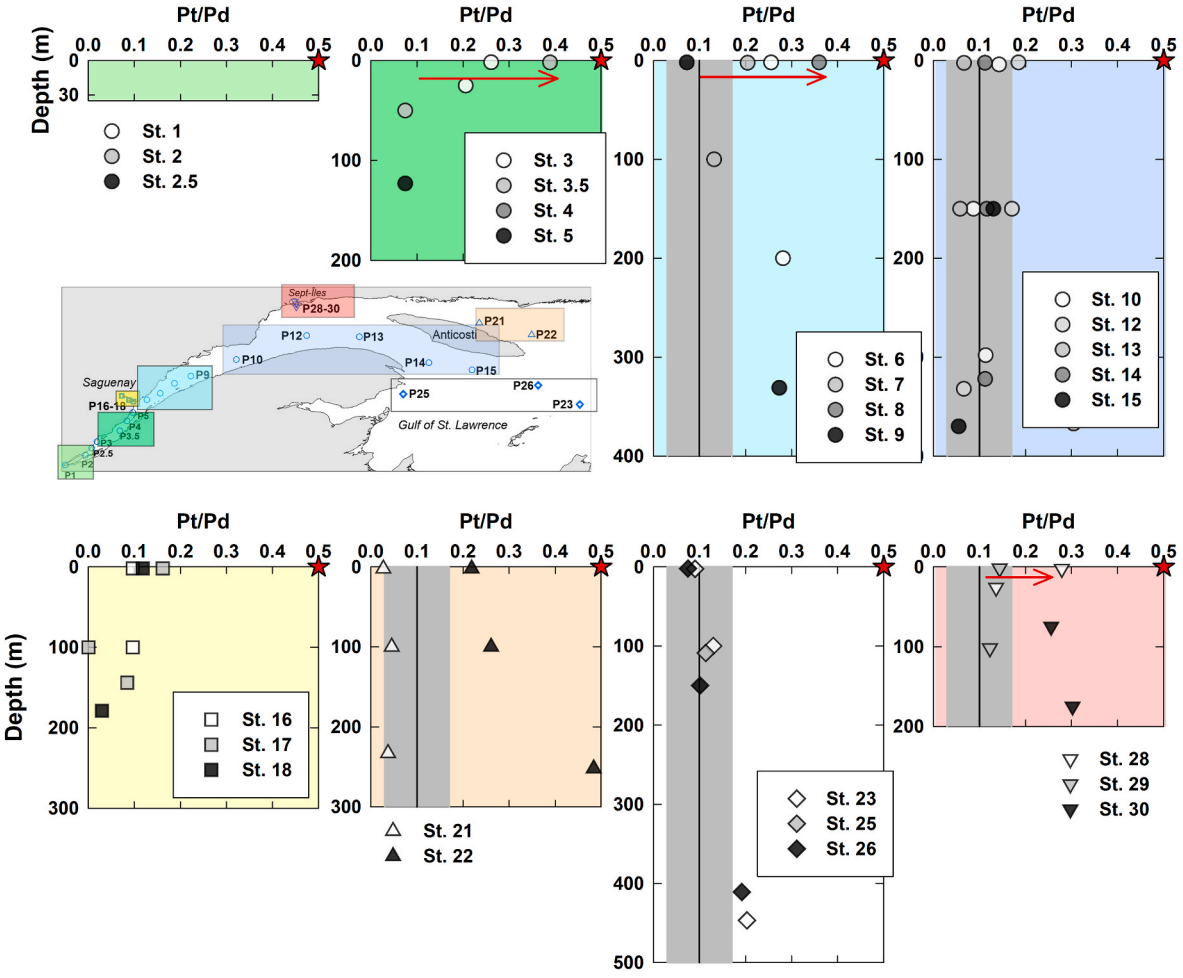

Fig. 7. Vertical profiles of molar Pt/Pd ratios categorized based on their locations within the EGSL. The vertical line and grey areas highlight the Pt/Pd ratios of the assumed oceanic end-member (0.10 ± 0.07), see text for more details. The red star identifies the atmospheric particle end-member, and the red arrows identify the surface samples with Pt/Pd ratios deviating towards the atmospheric source composition. Note that data in the river section (Stations 1, 2 and 2.5) are not available. (For interpretation of the references to colour in this figure legend, the reader is referred to the Web version of this article.)

4. Conclusion

The analysis of Ag, Pd and other trace elements in the surface waters of the EGSL during the winter of 2020 highlight their contrasting estuarine mixing behaviours. Most displayed near-conservative mixing behaviours (e.g., Cd, Re), that we ascribe to the limited flux or temporal variability in the particle size distribution of reactive particles to the estuary from the frozen watershed and ice cover during this season. Nevertheless, there were positive deviations of Ag and Pd concentrations from the conservative mixing line, particularly at the mid-salinity range ($15 < S_P < 20$), as reported from other estuarine systems. Their disparate behaviours are believed to reflect their differential sorption mechanisms to particulate surfaces, as previously demonstrated in laboratory mixing experiments for Pd and Pt.

In addition to the difference between the continental and oceanic end-member concentrations along the EGSL, we also observed distinct increases in the concentrations of several elements (Ag, Cr, Ni, Pb, Pd) within the Gulf of St. Lawrence, especially along its northern shores. Whereas there is insufficient sampling resolution to identify specific sources, they likely originate from the erosion of the chromite and nickeliferous mineral-rich watershed of Newfoundland and their anthropogenic enrichment in the sediment of Sept-Iles Bay. Both could serve as sources for these trace elements in the waters of the GSL.

The isolated and oxygen-depleted deep (>150 m) waters of the EGSL are characterized by a further and gradual loss of dissolved oxygen as they flow landward from Cabot Strait. Oxygen depletion within the EGSL results from the aerobic, microbial mineralization of organic matter that settles through the water column and accumulates in the sediments. Using a conventional T-S diagram and $\delta^{18}O–H_2O$ data, we identified the source waters to the EGSL and used the apparent oxygen utilization and $\delta^{13}C$-DIC to quantify the extent of OM respiration, as both are strongly correlated. The aerobic respiration of OM at depth may trigger the remobilization of elements strongly bound to particulate organic matter or whose redox speciation is altered at low oxygen levels in the water column or the sediment. The intermediate and deep-water concentrations of three of the studied elements (Cd, Cu, Re) fall on their surface-water mixing lines but most of the studied elements exhibit a significant enrichment (Ag, Pd, Cr, Ni, Pb and Zn) at depth.

The strong correlation between dissolved Pt concentrations and the AOU ($\delta^{13}C$-DIC and DIC) suggests that its remobilization is related to organic matter remineralization. The latter does not affect the geochemistry of Ag and only weakly influences Pd mobility. Assuming that the molar Pt/Pd signature (0.10 ± 0.07) of the oceanic water masses entering the GSL is preserved, the Pt/Pd in the surface water of the EGSL is likely strongly affected by the atmospheric deposition of particles emitted from road traffic whose Pt/Pd is 0.5–0.6. Nevertheless, further studies are required to constrain the signatures of continental waters, e.g., the Great Lakes and the St. Lawrence fluvial section.

CRediT authorship contribution statement

Duc Huy Dang: Writing – review & editing, Writing – original draft, Visualization, Investigation, Funding acquisition, Formal analysis, Data curation, Conceptualization. **Wei Wang:** Writing – review & editing, Methodology, Formal analysis, Conceptualization. **Dario Omanović:** Writing – review & editing, Methodology, Investigation, Formal analysis. **Alfonso Mucci:** Writing – review & editing, Methodology, Investigation, Conceptualization.

Declaration of competing interest

The authors declare that they have no known competing financial interests or personal relationships that could have appeared to influence the work reported in this paper.

Data availability

Data will be made available on request.

Acknowledgements

The authors acknowledge the financial support by NSERC Discovery grants to D.D.H and A.M. We are thankful to the captain and crew of the *CCGS Amundsen* and the chief scientist (Dr. Jean-Carlos Montero-Serrano). The authors also acknowledge the Réseau Québec Maritime and Programme Odyssée Saint-Laurent for the ship-time, as well as Maxence St-Onge and Erwann Fraboulet for logistic support. We wish to thank Jean-François Hélie at the GEOTOP Light Stable Isotope Geochemistry Laboratory (Université du Québec à Montréal) and research scientists at the Trent University Water Quality Centre.

Appendix A. Supplementary data

Supplementary data to this article can be found online at https://doi.org/10.1016/j.chemosphere.2024.142935.

References

Abdou, M., Gil-Díaz, T., Schäfer, J., Catrouillet, C., Bossy, C., Dutruch, L., Blanc, G., Cobelo-García, A., Massa, F., Castellano, M., Magi, E., Povero, P., Tercier-Waeber, M. Lou, 2020. Short-term variations of platinum concentrations in contrasting coastal environments: the role of primary producers. Mar. Chem. 222, 103782 https://doi.org/10.1016/j.marchem.2020.103782.

Barbante, C., Veysseyre, A., Ferrari, C., Van De Velde, K., Morel, C., Capodaglio, G., Cescon, P., Scarponi, G., Boutron, C., 2001. Greenland snow evidence of large scale atmospheric contamination for platinum, palladium, and rhodium. Environ. Sci. Technol. 35, 835–839. https://doi.org/10.1021/es000146y.

Barth, J.A.C., Veizer, J., 1999. Carbon cycle in St. Lawrence aquatic ecosystems at cornwall (Ontario), canda: seasonal and spatial variations. Chem. Geol. 159, 107–128. https://doi.org/10.1016/S0009-2541(99)00036-4.

Bazzano, A., Cappelletti, D., Udisti, R., Grotti, M., 2016. Long-range transport of atmospheric lead reaching Ny-Ålesund: inter-annual and seasonal variations of potential source areas. Atmos. Environ. 139, 11–19. https://doi.org/10.1016/j.atmosenv.2016.05.026.

Block, B.D., Denfeld, B.A., Stockwell, J.D., Flaim, G., Grossart, H.P.F., Knoll, L.B., Maier, D.B., North, R.L., Rautio, M., Rusak, J.A., Sadro, S., Weyhenmeyer, G.A., Bramburger, A.J., Branstrator, D.K., Salonen, K., Hampton, S.E., 2019. The unique methodological challenges of winter limnology. Limnol Oceanogr. Methods 17, 42–57. https://doi.org/10.1002/lom3.10295.

Bouillon, S., Connolly, R.M., Gillikin, D.P., 2012. Use of Stable Isotopes to Understand Food Webs and Ecosystem Functioning in Estuaries, Treatise on Estuarine and Coastal Science. Elsevier Inc. https://doi.org/10.1016/B978-0-12-374711-2.00711-7.

Braune, B., Chételat, J., Amyot, M., Brown, T., Clayden, M., Evans, M., Fisk, A., Gaden, A., Girard, C., Hare, A., Kirk, J., Lehnherr, I., Letcher, R., Loseto, L., Macdonald, R., Mann, E., McMeans, B., Muir, D., O'Driscoll, N., Poulain, A., Reimer, K., Stern, G., 2015. Mercury in the marine environment of the Canadian Arctic: review of recent findings. Sci. Total Environ. 509–510, 67–90. https://doi.org/10.1016/j.scitotenv.2014.05.133.

Chen, C., Sedwick, P.N., Sharma, M., 2009. Anthropogenic osmium in rain and snow reveals global-scale atmospheric contamination. Proc. Natl. Acad. Sci. U. S. A. 106, 7724–7728. https://doi.org/10.1073/pnas.0811803106.

Chételat, J., McKinney, M.A., Amyot, M., Dastoor, A., Douglas, T.A., Heimbürger-Boavida, L.E., Kirk, J., Kahilainen, K.K., Outridge, P.M., Pelletier, N., Skov, H., St Pierre, K., Vuorenmaa, J., Wang, F., 2022. Climate change and mercury in the Arctic: abiotic interactions. Sci. Total Environ. 824 https://doi.org/10.1016/j.scitotenv.2022.153715.

Claret, M., Galbraith, E.D., Palter, J.B., Bianchi, D., Fennel, K., Gilbert, D., Dunne, J.P., 2018. Rapid coastal deoxygenation due to ocean circulation shift in the northwest Atlantic. Nat. Clim. Change 8, 868–872. https://doi.org/10.1038/s41558-018-0263-1.

Cobelo-García, A., López-Sánchez, D.E., Schäfer, J., Petit, J.C.J., Blanc, G., Turner, A., 2014. Behavior and fluxes of Pt in the macrotidal Gironde estuary (SW France). Mar. Chem. 167, 93–101. https://doi.org/10.1016/j.marchem.2014.07.006.

Cobelo-Garcia, A., Turner, A., Millward, G.E., 2008. Fractionation and reactivity of platinum group elements during estuarine mixing. Environ. Sci. Technol. 42, 1096–1101. https://doi.org/10.1021/es0712118.

Colodner, D.C., 1991. The Marine Geochemistry of Rhenium, Iridium and Platinum. Massachusetts Institute of Technology.

Colodner, D.C., Boyle, E.A., Edmond, J.M., 1993. Determination of rhenium and platinum in natural waters and sediments, and iridium in sediments by flow injection isotope dilution inductively coupled plasma mass spectrometry. Anal. Chem. 65, 1419–1425. https://doi.org/10.1021/ac00058a019.

Cool, J., 2022. Étude de La dynamique de L'oxygène dans les sédiments du chenal laurentien. Universite du Quebec a Rimouski.
Dabrin, A., Schäfer, J., Blanc, G., Strady, E., Masson, M., Bossy, C., Castelle, S., Girardot, N., Coynel, A., 2009. Improving estuarine net flux estimates for dissolved cadmium export at the annual timescale: application to the Gironde Estuary. Estuar. Coast Shelf Sci. 84, 429–439. https://doi.org/10.1016/j.ecss.2009.07.006.
Dang, D.H., Omanović, D., Mucci, A., Wang, W., Sikma, A., Chatzis, A., 2022a. The winter estuarine geochemistry of platinum in the Estuary and Gulf of St . Lawrence. Mar. Chem. 242, 104123.
Dang, D.H., Wang, W., Sikma, A., Chatzis, A., Mucci, A., 2022b. The contrasting estuarine geochemistry of REEs between ice-covered and ice-free conditions. Geochem. Cosmochim. Acta 317, 488–506.
Delaigue, L., Thomas, H., Mucci, A., 2020. Spatial variations in CO2 fluxes in the Saguenay Fjord (Quebec, Canada) and results of a water mixing model. Biogeosciences. https://doi.org/10.5194/bg-17-547-2020.
Dinauer, A., Mucci, A., 2018. Distinguishing between physical and biological controls on the spatial variability of pCO2: a novel approach using OMP water mass analysis (St. Lawrence, Canada). Mar. Chem. 204, 107–120. https://doi.org/10.1016/j.marchem.2018.03.007.
El-Sabh, M., Silverberg, N., 1990. The St. Lawrence estuary: introduction. In: El-Sabh, M., Silverberg, N. (Eds.), Oceanography of a Large-Scale Estuarine System. Springer-Verlag, New York, pp. 1–9.
Fabris, A.S., Larouche, P., Montero-Serrano, J.C., 2021. Characterization of suspended matter size and composition in the St. Lawrence Estuary (eastern Canada). Reg. Stud. Mar. Sci. 45, 101838 https://doi.org/10.1016/j.rsma.2021.101838.
Fischer, L., Smith, G., Hann, S., Bruland, K.W., 2018. Ultra-trace analysis of silver and platinum in seawater by ICP-SFMS after off-line matrix separation and pre-concentration. Mar. Chem. 199, 44–52. https://doi.org/10.1016/j.marchem.2018.01.006.
Fischer, P., Dietrich, P., Achterberg, E.P., Anselm, N., Brix, H., Bussmann, I., Eickelmann, L., Flöser, G., Friedrich, M., Rust, H., Schütze, C., Koedel, U., 2021. Effects of measuring devices and sampling strategies on the interpretation of monitoring data for long-term trend analysis. Front. Mar. Sci. 8, 1–18. https://doi.org/10.3389/fmars.2021.770977.
Galbraith, P., Chassé, J., Shaw, J.L., Dumas, J., Caverhill, C., Lefaivre, D., Lafleur, C., 2021. Physical oceanographic conditions in the Gulf of St. Lawrence during 2020. DFO Can. Sci. Advis. Sec. Res. Doc.
Galbraith, P.S., 2006. Winter water masses in the Gulf of St. Lawrence. J. Geophys. Res. Ocean. 11, C06022 https://doi.org/10.1029/2005JC003159.
Garcia, H.E., Gordon, L.I., 1992. Oxygen solubility in seawater: better fitting equations. Limnol. Oceanogr. 37, 1307–1312. https://doi.org/10.4319/lo.1992.37.6.1307.
Gendron, A., Silverberg, N., Sundby, B., Lebel, J., 1986. Early diagenesis of cadmium and cobalt in sediments of the Laurentian Trough. Geochem. Cosmochim. Acta 50, 741–747. https://doi.org/10.1016/0016-7037(86)90350-9.
Gilbert, D., Sundby, B., Gobeil, C., Mucci, A., Tremblay, G.H., 2005. A seventy-two-year record of diminishing deep-water oxygen in the St. Lawrence estuary: the northwest Atlantic connection. Limnol. Oceanogr. 50, 1654–1666. https://doi.org/10.4319/lo.2005.50.5.1654.
Gobeil, C., Silverberg, N., 1989. Early diagenesis of lead in Laurentian Trough sediments. Geochem. Cosmochim. Acta 53, 1889–1895. https://doi.org/10.1016/0016-7037(89)90310-4.
Gobeil, C., Silverberg, N., Sundby, B., Cossa, D., 1987. Cadmium diagenesis in laurentian trough sediments. Geochem. Cosmochim. Acta 51, 589–596. https://doi.org/10.1016/0016-7037(87)90071-8.
Grasshoff, K., Kremling, K., Ehrhardt, M., 1999. Methods of Seawater Analysis, Third Edition, Methods of Seawater Analysis, third ed. Wiley-VCH.
Hélie, J.F., Hillaire-Marcel, C., Rondeau, B., 2002. Seasonal changes in the sources and fluxes of dissolved inorganic carbon through the St. Lawrence River - isotopic and chemical constraint. Chem. Geol. 186, 117–138. https://doi.org/10.1016/S0009-2541(01)00417-X.
INREST, 2013. Observatoire de veille environnementale de la baie de Sept-Iles - Phase I.
Ji, W., 2019. A Study of the Inorganic Carbon Cycling on the Scotian Shelf. Dalhousie University.
Jutras, M., Dufour, C.O., Mucci, A., Cyr, F., Gilbert, D., 2020. Temporal changes in the causes of the observed oxygen decline in the St. Lawrence Estuary. J. Geophys. Res. Ocean. 125, ee2020JC016577 https://doi.org/10.1029/2020jc016577.
Jutras, M., Dufour, C.O., Mucci, A., Talbot, L.C., 2023a. Large-scale control of the retroflection of the labrador current. Nat. Commun. 14 https://doi.org/10.1038/s41467-023-38321-y.
Jutras, M., Mucci, A., Chaillou, G., Nesbitt, W.A., Wallace, D.W.R., 2023b. Temporal and spatial evolution of bottom-water hypoxia in the St Lawrence estuarine system. Biogeosciences 20, 839–849. https://doi.org/10.5194/bg-20-839-2023.
Kreyling, J., Grant, K., Hammerl, V., Arfin-Khan, M.A.S., Malyshev, A.V., Peñuelas, J., Pritsch, K., Sardans, J., Schloter, M., Schuerings, J., Jentsch, A., Beierkuhnlein, C., 2019. Winter warming is ecologically more relevant than summer warming in a cool-temperate grassland. Sci. Rep. 9, 1–9. https://doi.org/10.1038/s41598-019-51221-w.
Lanceleur, L., Schäfer, J., Blanc, G., Coynel, A., Bossy, C., Baudrimont, M., Glé, C., Larrose, A., Renault, S., Strady, E., 2013. Silver behaviour along the salinity gradient of the Gironde Estuary. Environ. Sci. Pollut. Res. 20, 1352–1366. https://doi.org/10.1007/s11356-012-1045-3.
Lee, D.S., 1983. Palladium and nickel in north-east Pacific waters. Nature 305, 47–48. https://doi.org/10.1038/305047a0.
Lefort, S., Mucci, A., Sundby, B., 2012. Sediment response to 25 Years of persistent hypoxia. Aquat. Geochem. 18, 461–474.
Liu, K., Gao, X., Li, L., Chen, C.T.A., Xing, Q., 2018. Determination of ultra-trace Pt, Pd and Rh in seawater using an off-line pre-concentration method and inductively coupled plasma mass spectrometry. Chemosphere 212, 429–437. https://doi.org/10.1016/j.chemosphere.2018.08.098.
López-Sánchez, D.E., Cobelo-García, A., Rijkenberg, M.J.A., Gerringa, L.J.A., de Baar, H. J.W., 2019. New insights on the dissolved platinum behavior in the Atlantic Ocean. Chem. Geol. 511, 204–211. https://doi.org/10.1016/j.chemgeo.2019.01.003.
Loring, D.H., 1979. Geochemistry of cobalt, nickel, chromium, and vanadium in the sediments of the estuary and open Gulf of St. Lawrence. Can. J. Earth Sci. 16, 1196–1209.
Mashio, A.S., Ichimura, A., Yamagishi, H., Wong, K.H., Obata, H., Hasegawa, H., 2022a. Determination of the sub-picomolar concentration of dissolved palladium in open ocean seawater. Mar. Chem. 243, 104124 https://doi.org/10.1016/j.marchem.2022.104124.
Mashio, A.S., Ichimura, A., Yamagishi, H., Wong, K.H., Obata, H., Hasegawa, H., 2022b. Determination of the sub-picomolar concentration of dissolved palladium in open ocean seawater. Mar. Chem. 243, 104124 https://doi.org/10.1016/j.marchem.2022.104124.
McConnell, J.R., Chellman, N.J., Wilson, A.I., Stohl, A., Arienzo, M.M., Eckhardt, S., Fritzsche, D., Kipfstuhl, S., Opel, T., Place, P.F., Steffensen, J.P., 2019. Pervasive Arctic lead pollution suggests substantial growth in medieval silver production modulated by plague, climate, and conflict. Proc. Natl. Acad. Sci. U. S. A. 116, 14910–14915. https://doi.org/10.1073/pnas.1904515116.
Moldovan, M., Veschambre, S., Amouroux, D., Bénech, B., Donard, O.F.X., 2007. Platinum, palladium, and rhodium in fresh snow from the aspe valley (pyrenees mountains, France). Environ. Sci. Technol. 41, 66–73. https://doi.org/10.1021/es061483v.
Monteiro, C.E., Cobelo-García, A., Correia dos Santos, M.M., Caetano, M., 2021. Drivers of Rh and Pt variability in the water column of a hydrodynamic estuary: effects of contrasting environments. Sci. Total Environ. 760, 143909 https://doi.org/10.1016/j.scitotenv.2020.143909.
Nesbitt, W.A., Chaillou, G., Mucci, A., Tanhua, T., Wallace, D.W.R., 2024. Navigating a Continuum: the transport and transformation of dissolved inorganic carbon in the bottom waters of the St. Lawrence Estuary and Gulf. In: Ocean Sciences Meeting. New Orleans, Louisiana, U.S.A.
Nesbitt, W.A., Normandeau, C., Herard, O., Chaillou, G., Wallace, D., Mucci, A., 2023. Dynamics and sources of inorganic carbon in the bottom-waters of the Gulf of St. Lawrence, Canada. In: CMOS-SCMO Annual Congress. St-John's, Newfoundland, Canada.
Oldham, V.E., Siebecker, M.G., Jones, M.R., Mucci, A., Tebo, B.M., Luther, G.W., 2019. The speciation and mobility of Mn and Fe in estuarine sediments. Aquat. Geochem. 25, 3–26. https://doi.org/10.1007/s10498-019-09351-0.
Rauch, S., Hemond, H.F., Barbante, C., Owari, M., Morrison, G.M., Peucker-Ehrenbrink, B., Wass, U., 2005a. Importance of automobile exhaust catalyst emissions for the deposition of platinum, palladium, and rhodium in the northern hemisphere. Environ. Sci. Technol. 39, 8156–8162. https://doi.org/10.1021/es050784m.
Rauch, S., Hemond, H.F., Peucker-Ehrenbrink, B., Ek, K.H., Morrison, G.M., 2005b. Platinum group element concentrations and osmium isotopic composition in urban airborne particles from Boston, Massachusetts. Environ. Sci. Technol. 39, 9464–9470. https://doi.org/10.1021/es051310q.
Rauch, S., Peucker-Ehrenbrink, B., Molina, L.T., Molina, M.J., Ramos, R., Hemond, H.F., 2006. Platinum group elements in airborne particles in Mexico city. Environ. Sci. Technol. 40, 7554–7560. https://doi.org/10.1021/es061470h.
Rivera-Duarte, I., Flegal, A.R., Sañudo-Wilhelmy, S.A., Véron, A.J., 1999. Silver in the far North Atlantic ocean. Deep. Res. Part II Top. Stud. Oceanogr. 46, 979–990. https://doi.org/10.1016/S0967-0645(99)00012-0.
Silverberg, N., Sundby, B., 1979. Observations in the turbidity maximum of the St. Lawrence estuary. Can. J. Earth Sci. 16, 939–950. https://doi.org/10.1139/e79-080.
Sundby, B., Silverberg, N., Chesselet, R., 1981. Pathways of manganese in an open estuarine system. Geochem. Cosmochim. Acta 45, 293–307. https://doi.org/10.1016/0016-7037(81)90240-4.
Toggweiler, J.R., Russell, J., 2008. Ocean circulation in a warming climate. Nature 451, 286–288. https://doi.org/10.1038/nature06590.
Turner, A., 2007. Particle–water interactions of platinum group elements under estuarine conditions. Mar. Chem. 103, 103–111. https://doi.org/10.1016/j.marchem.2006.08.002.
Turner, A., Crussell, M., Millward, G.E., Cobelo-Garcia, A., Fisher, A.S., 2006. Adsorption kinetics of platinum group elements in river water. Environ. Sci. Technol. 40, 1524–1531. https://doi.org/10.1021/es0518124.
Waeles, M., Tanguy, V., Riso, R.D., 2014. High-resolution examination of the colloidal speciation of cadmium in estuarine waters (Penzé, NW France). Mar. Chem. 167, 71–81. https://doi.org/10.1016/j.marchem.2014.05.001.
Wang, W., Ma, L., Evans, R.D., Babechuk, M.G., Dang, D.H., 2022. Quantification of Re and four other trace elements (Ag, Cd, Pd, Zn) in certified reference materials and natural waters. J. Anal. At. Spectrom. 37, 1471–1483. https://doi.org/10.1039/d2ja00073c.
Whitney, N.M., Wanamaker, A.D., Switzer, M.E., Pettigrew, N.R., 2020. Using stable isotopes as tracers of water masses and nutrient cycling processes in the Gulf of Maine. Continent. Shelf Res. 206, 104210 https://doi.org/10.1016/j.csr.2020.104210.

Wiseman, C.L.S., Hassan Pour, Z., Zereini, F., 2016. Platinum group element and cerium concentrations in roadside environments in Toronto, Canada. Chemosphere 145, 61–67. https://doi.org/10.1016/j.chemosphere.2015.11.056.

Yang, C., Telmer, K., Veizer, J., 1996. Chemical dynamics of the "St. Lawrence" riverine system: δDH2O, δ18OH2O, δ13CDIC, δ34Ssulfate, and dissolved 87Sr/86Sr. Geochem. Cosmochim. Acta 60, 851–866. https://doi.org/10.1016/0016-7037(95)00445-9.

Yeghicheyan, D., Aubert, D., Bouhnik-Le Coz, M., Chmeleff, J., Delpoux, S., Djouraev, I., Granier, G., Lacan, F., Piro, J.L., Rousseau, T., Cloquet, C., Marquet, A., Menniti, C., Pradoux, C., Freydier, R., Vieira da Silva-Filho, E., Suchorski, K., 2019. A new interlaboratory characterisation of silicon, rare earth elements and twenty-two other trace element concentrations in the natural river water certified reference material SLRS-6 (NRC-CNRC). Geostand. Geoanal. Res. 43, 475–496. https://doi.org/10.1111/ggr.12268.